

RESEARCH ARTICLE

An optimal complexity spectral method for Navier–Stokes simulations in the ball

Nicolas Boullé¹ | Jonasz Słomka² | Alex Townsend³

¹Mathematical Institute, University of Oxford, Oxford, UK

²Institute for Environmental Engineering, Department of Civil, Environmental and Geomatic Engineering, ETH Zürich, Zürich, Switzerland

³Department of Mathematics, Cornell University, Ithaca, NY, USA

Correspondence

Nicolas Boullé, Mathematical Institute, University of Oxford, Oxford, UK.

Email: boulle@maths.ox.ac.uk

Summary

We develop a spectral method for solving the incompressible generalized Navier–Stokes equations in the ball with no-flux and prescribed slip boundary conditions. The algorithm achieves an optimal complexity per time step of $\mathcal{O}(N \log^2(N))$, where N is the number of spatial degrees of freedom. The method relies on the poloidal-toroidal decomposition of solenoidal vector fields, the double Fourier sphere method, the Fourier and ultraspherical spectral method, and the spherical harmonics transform to decouple the Navier–Stokes equations and achieve the desired complexity and spectral accuracy.

KEYWORDS:

computational fluid dynamics, Navier–Stokes equations, spectral method, poloidal-toroidal decomposition, integral conditions, spherical harmonics

1 | INTRODUCTION

Complex fluids, such as active fluids in biology and quantum fluids in physics, are often modeled by Navier–Stokes-like equations. Computational techniques for simulating these fluids in realistic configurations found in laboratories, such as cylinders, balls, and ellipsoids, are critical for experimental design. In this paper, we develop a new optimal-complexity spectral method for their simulation. In particular, we consider the generalized Navier–Stokes (NS) equations, which have been used to model active fluids^{1,2}:

$$\nabla \cdot \mathbf{v} = 0, \quad (1a)$$

$$\partial_t \mathbf{v} + \mathbf{v} \cdot \nabla \mathbf{v} = -\nabla p + \nabla \cdot \boldsymbol{\sigma}, \quad (1b)$$

defined on the unit ball $\Omega = \overline{B(0, 1)}$ with velocity boundary conditions tangent to the surface of the sphere, i.e. $\mathbf{v}|_{\partial\Omega} \cdot \hat{\mathbf{r}} = 0$, where $\hat{\mathbf{r}}$ is the unit radial direction. Here, $\mathbf{v}(t, x)$ is the fluid velocity and $p(t, x)$ the local pressure, where $t \geq 0$ and $x \in \overline{B(0, 1)}$. In this work, we consider the stress tensor $\boldsymbol{\sigma}(t, x)$ to be defined as

$$\boldsymbol{\sigma} = (\Gamma_0 - \Gamma_2 \nabla^2 + \Gamma_4 \nabla^4)[\nabla \mathbf{v} + (\nabla \mathbf{v})^\top], \quad (2)$$

with higher order derivatives $\nabla^{2n} = (\nabla^2)^n$ for $n \geq 2$ stimulating non-Newtonian effects. When $\Gamma_2 = \Gamma_4 = 0$, Eq. (1) reduces to the incompressible NS equations with Reynolds number $Re = 1/\Gamma_0$.

Standard approaches for numerically solving the incompressible NS equations use primitive variables to solve for the fluid's velocity and pressure directly. One of the main difficulties with this formulation is ensuring that the computed velocity vector remains exactly, or even approximately, divergence-free. Typically, projection-based schemes are used to enforce this condition^{3,4}. Still, these can lead to difficulties with boundary conditions and reduce temporal accuracy⁵. A novel approach is taken by the Dedalus software project, where the full-ball spectral code implicitly imposes incompressibility of the fluid in the coupled

formulation^{6,7} and ensures regularity of the solution using one-side Jacobi bases⁸. Another approach that appears in numerous spectral solvers^{9,10,11,12}, and the approach that we use in this paper, is to reformulate the NS equations using a poloidal-toroidal (PT) decomposition. This technique reduces the fully coupled NS system for the velocity and pressure to two coupled equations for the poloidal and toroidal scalar fields and has numerous computational benefits: (i) There can be a significant computational saving as only scalar fields need to be computed; (ii) Vector-valued PDEs are reduced to scalar-valued PDEs, allowing for fast PDE solvers and a parallel implementation; and (iii) The poloidal-toroidal decomposition^{13,14,15} explicitly enforces incompressibility of the fluid velocity vector without the need for projection-based methods. One of our novelties, is to impose the boundary conditions for the velocity using equivalent integral conditions¹⁶ on the poloidal and toroidal scalars of the vorticity, which allows us to completely decouple the equations and achieve optimal complexity of the spectral solver at each time-step with respect to the spatial discretization.

In this paper, we describe an algorithm for solving the generalized NS equations, which achieves both spectral accuracy and optimal complexity per time step $\mathcal{O}(N \log^2(N))$ with respect to the number of degrees of freedom N . We refer to optimal complexity as an asymptotically linear complexity up to polylogarithmic factors of N . In addition to the poloidal-toroidal decomposition mentioned above, the numerical method relies on three ideas for discretizing the equations: (1) The extension of the double Fourier sphere (DFS) method to the ball¹⁷, which allows for fast computations with functions and vector fields such as vector calculus operations. (2) A spherical harmonics basis for solving the partial differential equations resulting from the PT decomposition of the NS equations. (3) The ultraspherical spectral method¹⁸ for performing optimal complexity mathematical operations (such as differentiation and solving PDEs) with respect to the radial variable, which relies on the relations between Chebyshev and ultraspherical polynomials. There are several significant benefits to using global spectral methods for Eq. (1): (a) Superior approximations of high-order derivatives that appear in Eq. (1), (b) better spatial resolution of advection-dominated fluids, (c) more accurate long-time simulations (by avoiding artificial diffusion), and (d) robust bulk-boundary fluid interactions.

This paper is organized as follows. In Section 2, we use the poloidal-toroidal decomposition to decouple the NS equations and enforce boundary conditions. Then, in Section 3, we describe the spectral discretization and associated numerical solvers for solving the poloidal and toroidal equations. Finally, we provide numerical examples in Section 4 and conclude in Section 5.

2 | POLOIDAL-TOROIDAL FORMULATION OF THE NAVIER-STOKES EQUATIONS

2.1 | Vorticity formulation

We first express the NS equations in the vorticity-vector potential form. According to the Helmholtz-Hodge decomposition¹⁹, any divergence-free vector field \mathbf{v} in the ball can be decomposed as

$$\mathbf{v} = \nabla \times \boldsymbol{\psi} + \nabla \phi,$$

where the divergence-free vector potential $\boldsymbol{\psi}$ is normal to the boundary, $\boldsymbol{\psi} \times \hat{\mathbf{r}}|_{r=1} = 0$, and ϕ is a harmonic function. Note that no harmonic vector fields are present in the above formula since our domain is simply connected. The gradient $\nabla \phi$ is uniquely determined by the Neumann boundary conditions corresponding to the flux across the boundary $\mathbf{v} \cdot \hat{\mathbf{r}} = \nabla \phi \cdot \hat{\mathbf{r}}$. Since this gradient can be eliminated by setting $\tilde{\mathbf{v}} = \mathbf{v} - \nabla \phi$, from now on we consider the special case

$$\mathbf{v} = \nabla \times \boldsymbol{\psi},$$

where \mathbf{v} is tangent to the boundary. Taking curl of the generalized NS equations Eq. (1) yields the vorticity-vector potential formulation

$$\nabla^2 \boldsymbol{\psi} = -\boldsymbol{\omega}, \tag{3a}$$

$$(\partial_t - \Gamma_0 \nabla^2 + \Gamma_2 \nabla^4 - \Gamma_4 \nabla^6) \boldsymbol{\omega} = -\nabla \times (\boldsymbol{\omega} \times \mathbf{v}), \tag{3b}$$

where $\boldsymbol{\omega} = \nabla \times \mathbf{v}$ is the vorticity. In the next section, we decouple Eq. (3) by using a vector decomposition called the poloidal-toroidal decomposition.

2.2 | Reformulation of the NS equations with the PT decomposition

A divergence-free vector field $\boldsymbol{\psi}$ in spherical coordinates can be decomposed with the poloidal-toroidal (PT) decomposition into an orthogonal sum of a poloidal and toroidal field as¹³ $\boldsymbol{\psi} = \mathbf{P} + \mathbf{T}$. Moreover, there exist a poloidal and toroidal scalars: P_ψ and

T_ψ , unique up to the addition of an arbitrary function of the radial variable $r \in [0, 1]$ such that

$$\begin{aligned}\mathbf{P} &= \nabla \times \nabla \times (\mathbf{r} P_\psi) = -\mathbf{r} \nabla^2 P_\psi + \nabla [\partial_r (r P_\psi)], \\ \mathbf{T} &= \nabla \times (\mathbf{r} T_\psi),\end{aligned}$$

where $\mathbf{r} := r\hat{\mathbf{r}}$. Thanks to the above decomposition, we can write down the PT decomposition of the velocity and vorticity fields as

$$\mathbf{v} = \nabla \times \psi = \nabla \times \nabla \times (\mathbf{r} T_\psi) + \nabla \times (-\mathbf{r} \nabla^2 P_\psi), \quad (4a)$$

$$\boldsymbol{\omega} = \nabla \times \mathbf{v} = \nabla \times \nabla \times (-\mathbf{r} \nabla^2 P_\psi) + \nabla \times (-\mathbf{r} \nabla^2 T_\psi). \quad (4b)$$

We have found the action of the poloidal-toroidal decomposition under the transformation $\psi \rightarrow \nabla \times \nabla \times \psi$:

$$P_\psi \rightarrow -\nabla^2 P_\psi, \quad T_\psi \rightarrow -\nabla^2 T_\psi.$$

It follows from Eqs. (3a) and (4) and the orthogonality of the PT decomposition that the PT scalars for ψ and $\boldsymbol{\omega}$ obey two Poisson equations

$$\begin{aligned}\nabla^2 P_\psi &= -P_\omega, \\ \nabla^2 T_\psi &= -T_\omega.\end{aligned}$$

Then, the uniqueness of the poloidal and toroidal scalars up to the addition of a function of r and Eq. (4) implies that

$$\nabla^2 P_v = -T_\omega, \quad (5a)$$

$$T_v = P_\omega, \quad (5b)$$

where made the identifications $P_v = T_\psi$ and $T_v = -\nabla^2 P_\psi$. Additionally, P_v satisfies the Dirichlet boundary condition because ψ is normal to the boundary implying that T_ψ and thus P_v must vanish on the boundary.

We now turn to the PT decomposition of Eq. (3b) and derive the equations satisfied by the vorticity PT scalars (P_ω, T_ω) . Again, the orthogonality of the PT decomposition and Eq. (4) imply that (P_ω, T_ω) satisfy

$$(\partial_t - \Gamma_0 \nabla^2 + \Gamma_2 \nabla^4 - \Gamma_4 \nabla^6) P_\omega = -P_{\nabla \times (\boldsymbol{\omega} \times \mathbf{v})}, \quad (6a)$$

$$(\partial_t - \Gamma_0 \nabla^2 + \Gamma_2 \nabla^4 - \Gamma_4 \nabla^6) T_\omega = -T_{\nabla \times (\boldsymbol{\omega} \times \mathbf{v})}, \quad (6b)$$

where the right-hand sides correspond to the PT decomposition of the nonlinear term $\nabla \times (\boldsymbol{\omega} \times \mathbf{v})$.

2.3 | Boundary conditions

Since we focus on velocity fields \mathbf{v} that are tangent to the boundary, the most general boundary conditions for \mathbf{v} correspond to an arbitrary two-dimensional vector field \mathbf{v}^t on the unit sphere. We use the Hodge decomposition to represent \mathbf{v}^t as a sum of a surface gradient and a surface curl (skew-gradient):

$$\mathbf{v}|_{\partial\Omega} = \mathbf{v}^t = \nabla_1 f + \Lambda_1 g, \quad (7)$$

where f, g are two arbitrary functions on the unit sphere. Let $(\hat{\mathbf{r}}, \hat{\boldsymbol{\lambda}}, \hat{\boldsymbol{\theta}})$ be the unit vectors in spherical coordinates in the radial, azimuthal, and polar directions, then the surface gradient and curl are defined as

$$\nabla_1 f = \frac{1}{\sin \theta} \frac{\partial f}{\partial \lambda} \hat{\boldsymbol{\lambda}} + \frac{\partial f}{\partial \theta} \hat{\boldsymbol{\theta}}, \quad \Lambda_1 g = -\frac{\partial g}{\partial \theta} \hat{\boldsymbol{\lambda}} + \frac{1}{\sin \theta} \frac{\partial g}{\partial \lambda} \hat{\boldsymbol{\theta}}.$$

The two surface potentials f and g parametrize the compressible and irrotational part of \mathbf{v}^t , respectively, and are user-specified functions, which can be time-dependent.

2.3.1 | Dirichlet conditions for P_ω

We observe that the poloidal scalar P_ω obeys the following Dirichlet boundary condition:

$$P_\omega|_{\partial\Omega} = g(\lambda, \theta), \quad (8)$$

where g is the scalar potential of the irrotational part of the velocity field \mathbf{v}^t , $\lambda \in [-\pi, \pi]$ is the azimuthal variable, and $\theta \in [0, \pi]$ is the polar angle. This follows from Eqs. (4) and (7), which imply that $T_v(1, \lambda, \theta) = g(\lambda, \theta) = P_\omega(1, \lambda, \theta)$.

2.3.2 | Integral conditions for T_ω

Quartapelle and Valz-Gris¹⁶ showed that specifying the boundary conditions for the velocity field \mathbf{v} is equivalent to imposing integral conditions on the vorticity $\boldsymbol{\omega}$. The integral conditions take the form of projections of $\boldsymbol{\omega}$ onto the linear space of vector fields $\boldsymbol{\eta}$ that satisfy $\nabla \times \nabla \times \boldsymbol{\eta} = 0$. We first show that only half of these projections correspond to true integral conditions, and the other half is equivalent to specifying the normal component of $\boldsymbol{\omega}$.

Consider the linear space of vector fields $\boldsymbol{\eta}$ that satisfy $\nabla \times \nabla \times \boldsymbol{\eta} = 0$. Without loss of generality, we may assume that $\boldsymbol{\eta}$ is divergence-free. We apply the PT decomposition to $\boldsymbol{\eta}$ and note that $\nabla \times \nabla \times \boldsymbol{\eta} = -\nabla^2 \boldsymbol{\eta} = 0$ implies that the corresponding PT scalars are harmonic functions:

$$\nabla^2 P_\eta = 0, \quad \nabla^2 T_\eta = 0,$$

where again we employed the orthogonality of the PT decomposition to obtain two independent equations. Since P_η is harmonic, we immediately conclude that the poloidal fields \mathbf{P}_η are gradients of functions

$$\mathbf{P}_\eta = \nabla \times \nabla \times (\mathbf{r} P_\eta) = -\mathbf{r} \nabla^2 P_\eta + \nabla[\partial_r(r P_\eta)] = \nabla[\partial_r(r P_\eta)].$$

Moreover, since \mathbf{P}_η is divergence-free, it is a gradient of a harmonic function. Therefore, projecting $\boldsymbol{\omega}$ onto \mathbf{P}_η is equivalent to specifying the gradient part of the Hodge decomposition for $\boldsymbol{\omega}$, which in turn is fully determined by the normal component $\boldsymbol{\omega} \cdot \hat{\mathbf{r}}$. We conclude that one half of the integral conditions on $\boldsymbol{\omega}$ put forward by Quartapelle and Valz-Gris¹⁶ do not constitute true integral conditions in the sense that they are equivalent to boundary conditions. This equivalence is demonstrated by the fact that the poloidal scalar P_ω obeys the Dirichlet boundary conditions (8) rather than integral conditions. Physically, this means that the normal component of the vorticity is determined by the surface curl of the velocity field on the boundary.

We now show that the toroidal scalar T_ω obeys integral conditions. Consider projecting $\boldsymbol{\omega}$ onto toroidal fields $\mathbf{T}_\eta = \nabla \times (\mathbf{r} T_\eta)$, where T_η is a harmonic function. We obtain

$$\int_\Omega \boldsymbol{\omega} \cdot \mathbf{T}_\eta \, dx = \int_\Omega \mathbf{T}_\omega \cdot \mathbf{T}_\eta \, dx = \int_\Omega \nabla \times (\mathbf{r} T_\omega) \cdot \nabla \times (\mathbf{r} T_\eta) \, dx,$$

where we used the orthogonality of the PT decomposition. Integrating by parts yields

$$\int_\Omega \boldsymbol{\omega} \cdot \mathbf{T}_\eta \, dx = \int_\Omega T_\omega \mathbf{r} \cdot \nabla \times \nabla \times (\mathbf{r} T_\eta) \, dx = \int_\Omega T_\omega \mathbf{r} \cdot \{-\mathbf{r} \nabla^2 T_\eta + \nabla[\partial_r(r T_\eta)]\} \, dx = \int_\Omega T_\omega r \partial_{rr}(r T_\eta) \, dx,$$

where we used the fact that T_η is harmonic. We now show that the above true integral conditions are equivalent to specifying the compressible part of the two-dimensional flow fixed by the boundary conditions on the velocity field.

Consider the same integral conditions as above but now integrate by parts to convert $\boldsymbol{\omega}$ into \mathbf{v} by using $\boldsymbol{\omega} = \nabla \times \mathbf{v}$:

$$\int_\Omega \boldsymbol{\omega} \cdot \mathbf{T}_\eta \, dx = \int_\Omega \nabla \times \mathbf{v} \cdot \nabla \times (\mathbf{r} T_\eta) \, dx = \int_\Omega \nabla \cdot [\mathbf{v} \times \nabla \times (\mathbf{r} T_\eta)] \, dx + \int_\Omega \mathbf{v} \cdot \nabla \times \nabla \times (\mathbf{r} T_\eta) \, dx. \quad (9)$$

We first note that the second integral vanishes as

$$\int_\Omega \mathbf{v} \cdot \nabla \times \nabla \times (\mathbf{r} T_\eta) \, dx = \int_\Omega \mathbf{v} \cdot \nabla[\partial_r(r T_\eta)] \, dx = 0.$$

This follows from the orthogonality of the Hodge decomposition as the second integral above is the projection of \mathbf{v} onto gradients of functions while \mathbf{v} comes from the vector potential only. Going back to Eq. (9), we employ the divergence theorem

$$\int_\Omega \boldsymbol{\omega} \cdot \mathbf{T}_\eta \, dx = \int_\Omega \nabla \cdot [\mathbf{v} \times \nabla \times (\mathbf{r} T_\eta)] \, dx = \int_{\partial\Omega} \hat{\mathbf{r}} \cdot [\mathbf{v} \times \nabla \times (\mathbf{r} T_\eta)] \, ds.$$

We can use the triple product to rewrite the surface integral as

$$\hat{\mathbf{r}} \cdot [\mathbf{v} \times \nabla \times (\mathbf{r} T_\eta)] = -\mathbf{v} \cdot [\hat{\mathbf{r}} \times \nabla \times (\mathbf{r} T_\eta)] = -\mathbf{v} \cdot \nabla_1 T_\eta,$$

where ∇_1 is the surface gradient. The integral condition reads

$$\int_\Omega \boldsymbol{\omega} \cdot \mathbf{T}_\eta \, dx = - \int_{\partial\Omega} \mathbf{v} \cdot \nabla_1 T_\eta \, ds = - \int_{\partial\Omega} \nabla_1 f \cdot \nabla_1 T_\eta \, ds = \int_{\partial\Omega} f \nabla_1^2 T_\eta \, ds, \quad (10)$$

where in the second equality we used the orthogonality of the Hodge decomposition of velocity fields on the boundary and in the last equality we integrated by parts. We conclude that the true integral conditions, corresponding to the projections of the vorticity onto toroidal fields with harmonic toroidal scalars, fix the compressible part of the velocity field \mathbf{v}^t on the boundary parameterized by the surface potential f (cf. Section 2.3).

3 | NUMERICAL METHOD

In this section, we discuss the numerical method used to discretize the poloidal-toroidal formulation of the incompressible NS equations. We then wish to solve the following equations (see Section 2.2):

$$\begin{aligned}\nabla^2 P_v &= -T_\omega, \\ T_v &= P_\omega,\end{aligned}$$

with homogeneous Dirichlet boundary conditions on P_v . The second system of equations reads

$$(\partial_t - \Gamma_0 \nabla^2 + \Gamma_2 \nabla^4 - \Gamma_4 \nabla^6) P_\omega = -P_{\nabla \times (\omega \times v)}, \quad (11a)$$

$$(\partial_t - \Gamma_0 \nabla^2 + \Gamma_2 \nabla^4 - \Gamma_4 \nabla^6) T_\omega = -T_{\nabla \times (\omega \times v)}, \quad (11b)$$

with Dirichlet boundary conditions on P_ω (see Section 2.3.1) and integral conditions on T_ω according to Section 2.3.2. We discretize Eq. (11) in time using the implicit-explicit backward differentiation of order one (IMEX-BDF1) time-stepping scheme. In this paper, we focus on the optimal complexity spatial discretization and employ this time-stepping scheme for simplicity but higher order schemes may be more appropriate for solving the NS equations^{20,21,22,23}. Let Δt be the temporal discretization and $k \geq 0$ the current time-step of the algorithm. At step $k + 1$, assuming the scalars P_ω^k and T_ω^k have already been computed, we have to solve the following Poisson's equation with zero Dirichlet conditions:

$$\nabla^2 P_v^k = -T_\omega^k, \quad (12a)$$

$$T_v^k = P_\omega^k. \quad (12b)$$

Moreover, if we denote $\mathbf{N} = \nabla \times (\omega \times v)$, then Eq. (11) reads

$$(-\Gamma_0 \nabla^2 + \Gamma_2 \nabla^4 - \Gamma_4 \nabla^6) P_\omega^{k+1} + \frac{1}{\Delta t} P_\omega^{k+1} = \frac{1}{\Delta t} P_\omega^k - P_{\mathbf{N}}, \quad (13a)$$

$$(-\Gamma_0 \nabla^2 + \Gamma_2 \nabla^4 - \Gamma_4 \nabla^6) T_\omega^{k+1} + \frac{1}{\Delta t} T_\omega^{k+1} = \frac{1}{\Delta t} T_\omega^k - T_{\mathbf{N}}. \quad (13b)$$

We propose a fast algorithm to solve Eqs. (12)-(13) and thus achieve an optimal complexity solver to the NS equations per time step. Here, “optimal” denotes a linear complexity, up to polylogarithmic factors, in terms of the degrees of freedom needed to resolve the solution spatially. The poloidal and toroidal components of the vorticity and the velocity vector fields are approximated using a global spectral method, introduced in section 3.1. Our choice of spectral basis takes into account the existence of fast –FFT based– transforms between spectral coefficients and physical values space, which is needed to compute the nonlinear advection term in the NS equations since it is treated explicitly by our time-stepping scheme. This nonlinear vector field also requires a poloidal-toroidal decomposition algorithm and the ability to perform vector calculus operations (see Section 3.2). Finally, Section 3.3 consists of the description of a fast Helmholtz's solver with Dirichlet and integral conditions, used to numerically solve Eqs. (12) and (13) at every time-step. Fig. 1 summarizes the NS algorithm and shows the resulting optimal complexity per time step.

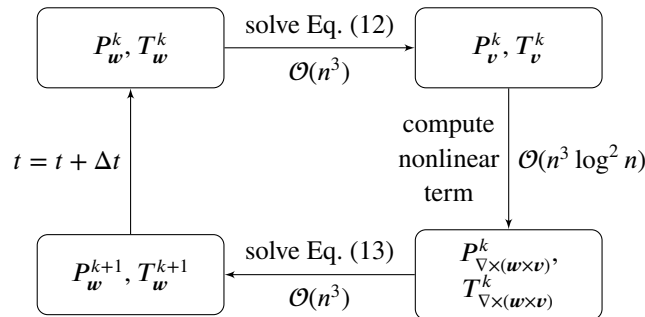


FIGURE 1 Tasks performed during one time-step of the NS solver with associated computational complexity. The poloidal and toroidal scalars P_w, T_w are discretized using $\mathcal{O}(n^3)$ physical values (n for each radial, azimuthal, and polar direction).

3.1 | Spatial discretization of functions and vectors on the ball

We now discuss the different polynomial basis employed to approximate functions and vector-valued functions defined on the ball, perform vector calculus operations, compute poloidal-toroidal decompositions and solve Helmholtz's equation.

3.1.1 | Chebyshev–Fourier–Fourier basis

If f is a smooth function on the ball, then it can be represented in a Chebyshev–Fourier–Fourier (CFF) series:

$$f(r, \lambda, \theta) \approx \sum_{k=0}^{+\infty} \sum_{l=-\infty}^{+\infty} \sum_{m=-\infty}^{+\infty} f_{klm} T_k(r) e^{il\lambda} e^{im\theta}, \quad (14)$$

where $(r, \lambda, \theta) \in [0, 1] \times [-\pi, \pi] \times [0, \pi]$ and T_k is the degree k Chebyshev polynomial of the first kind. The function f is discretized in $\mathcal{O}(n^3)$ coefficients by truncating the series (14),

$$f(r, \lambda, \theta) \approx \sum_{k=0}^{n/2} \sum_{l=-n/2}^{n/2} \sum_{m=-n/2}^{n/2} f_{klm} T_k(r) e^{il\lambda} e^{im\theta}, \quad (15)$$

where n is an even integer.

A few salient features make this discretization choice attractive for working with functions on the ball. First, any smooth function can be represented as in (15) using the double sphere method²⁴ to remove artificial boundary conditions at the poles and at the origin. This method, originally proposed by Merilees, has been extended to various tensor-product domains such as the sphere, the disk, and the ball^{17,25,26}. This method extends a function f defined on the ball to a function \tilde{f} defined on $[-1, 1] \times [-\pi, \pi] \times [-\pi, \pi]$. Moreover, the Chebyshev–Fourier–Fourier coefficients of \tilde{f} , (f_{klm}) , can be computed in $\mathcal{O}(n^3 \log n)$ operations by sampling f at the three dimensional Chebyshev–Fourier–Fourier grid

$$\left(\cos\left(\frac{2k\pi}{n}\right), \frac{2l\pi}{n}, \frac{2m\pi}{n} \right), \quad 0 \leq k \leq \frac{n}{2}, \quad -\frac{n}{2} \leq l, m \leq \frac{n}{2}, \quad (16)$$

and using transforms based on the FFT²⁷. Finally, operations such as differentiation, vector calculus, and computing the poloidal-toroidal decomposition of vector-valued functions can be done efficiently and are already in the package Ballfun¹⁷, which is a component of the Chebfun software²⁸.

3.1.2 | Chebyshev-Spherical harmonic basis

One can also approximate a smooth function f on the ball by the following expansion, called a Chebyshev-Spherical harmonic (CSH) series,

$$f(r, \lambda, \theta) \approx \sum_{k=0}^{+\infty} \sum_{l=0}^{+\infty} \sum_{m=-l}^l f_{klm} T_k(r) Y_l^m(\theta, \lambda). \quad (17)$$

The spherical harmonics Y_l^m are defined by $Y_l^m(\theta, \lambda) = \tilde{P}_l^m(\cos \theta) e^{im\lambda}$, where P_l^m is the normalized associated Legendre polynomials of degree l and order m such that

$$\int_{\partial\Omega} Y_l^m Y_{l'}^{m'*} ds = \delta_{ll'} \delta_{mm'},$$

where $\delta_{ll'} = 1$ if $l = l'$ and zero otherwise. The truncation of (17) to Chebyshev polynomials up to degree $n/2$ and wave frequencies up to order $n/2$ yields

$$f(r, \lambda, \theta) \approx \sum_{k=0}^{n/2} \sum_{l=0}^{n/2} \sum_{m=-l}^l f_{klm} T_k(r) Y_l^m(\theta, \lambda). \quad (18)$$

Slevinsky introduced a fast and practical algorithm, called the spherical harmonic transform (SHT), for transformations between spherical harmonic expansions and bivariate Fourier series²⁹. We use this algorithm to convert functions expressed in the CSH basis into the CFF basis in $\mathcal{O}(n^3 \log^2 n)$ operations. The inverse discrete cosine transform (DCT)^{30,31,32} and the fast Fourier transform²⁷ are then used to convert the CFF coefficients into values. The following diagram summarizes the operations used to evaluate a function expressed as a CSH series at the CFF points:

$$\text{CSH coefficients} \xleftrightarrow[\mathcal{O}(n^3 \log^2 n)]{\text{DCT+SHT}} \text{CFF coefficients} \xleftrightarrow[\mathcal{O}(n^3 \log n)]{\text{DCT+FFT}} \text{Values at CFF points.}$$

3.2 | Vector calculus and PT decomposition

In this section, we assume the existence of two functions P_v and T_v , representing the poloidal and toroidal scalars (see Section 2.2) of a divergence-free vector field \mathbf{v} in the CSH basis. These functions are approximated by a series of $\mathcal{O}(n^3)$ Chebyshev and spherical harmonics coefficients and the number of degrees of freedom needed to represent the three components of the velocity field \mathbf{v} is equal to $N = 3(n/2 + 1)(n + 1)^2 = \mathcal{O}(n^3)$. We then explain the computation the poloidal-toroidal decomposition of $\nabla \times (\boldsymbol{\omega} \times \mathbf{v})$, where $\boldsymbol{\omega}$ is a vector-valued function defined by $\boldsymbol{\omega} = \nabla \times \mathbf{v}$.

Given the functions P_v and T_v in the CSH basis, we first convert them to the CFF basis with the spherical harmonic transform (see Section 3.1.2) in $\mathcal{O}(n^3 \log^2 n)$ operations. According to Section 2.2, the vector-valued function \mathbf{v} can be recovered from its poloidal and toroidal scalars using vector calculus:

$$\mathbf{v} = \nabla \times \nabla \times (\mathbf{r} P_v) + \nabla \times (\mathbf{r} T_v).$$

This last operation is performed in optimal complexity, $\mathcal{O}(n^3)$, in the CFF basis¹⁷. The vector field $\boldsymbol{\omega} = \nabla \times \mathbf{v}$ is computed as well in $\mathcal{O}(n^3)$ operations using the expression of \mathbf{v} in the CFF basis. This allows us to perform only two forward SHTs (on the poloidal and toroidal scalars of \mathbf{v}) to compute \mathbf{v} and $\boldsymbol{\omega}$ in the CFF basis. We then sample the Cartesian components of \mathbf{v} and $\boldsymbol{\omega}$ with six fast transforms based on FFT in $\mathcal{O}(n^3 \log n)$ operations (see Section 3.1.1). The tensors representing the evaluation of \mathbf{v} and $\boldsymbol{\omega}$ at the CFF points are multiplied element-wise and transformed back into CFF coefficients to get an approximation of $\boldsymbol{\omega} \times \mathbf{v}$ as a CFF series. We then take the curl of $\boldsymbol{\omega} \times \mathbf{v}$ by doing vector calculus operations in the CFF basis. The next step is to compute the poloidal-toroidal decomposition of $\nabla \times \boldsymbol{\omega} \times \mathbf{v}$. A fast algorithm in $\mathcal{O}(n^3)$ operations is described in¹⁷ and returns the CFF coefficients of the poloidal and toroidal scalars $P_{\nabla \times (\boldsymbol{\omega} \times \mathbf{v})}$ and $T_{\nabla \times (\boldsymbol{\omega} \times \mathbf{v})}$. Finally, these functions, expressed as CFF series, are transformed in the CSH basis via an inverse SHT. Fig. 2 summarizes the algorithms used to compute the nonlinear term. Note that we expand the CFF series representing the Cartesian components of $\boldsymbol{\omega}$ and \mathbf{v} using the 3/2 rule to prevent aliasing effects during the computation of $\boldsymbol{\omega} \times \mathbf{v}$ ³³. Later, we truncate the nonlinear term to the original spatial discretization.

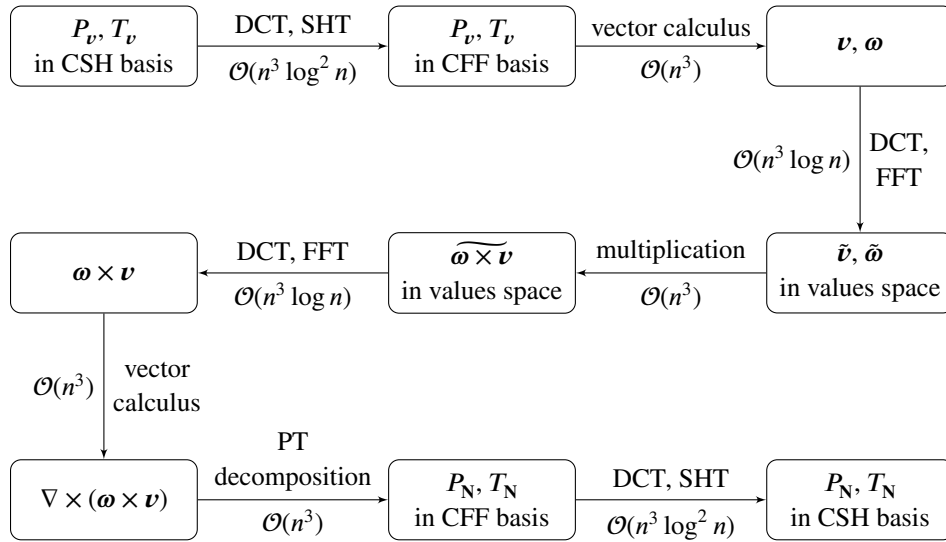


FIGURE 2 Procedure used to compute the poloidal-toroidal decomposition of the vector field $\mathbf{N} := \nabla \times (\boldsymbol{\omega} \times \mathbf{v})$ in the CSH basis. $\tilde{\mathbf{v}}$, $\tilde{\boldsymbol{\omega}}$, and $\tilde{\boldsymbol{\omega}} \times \tilde{\mathbf{v}}$ respectively denote the CFF values of the vector-valued functions \mathbf{v} , $\boldsymbol{\omega}$, and $\boldsymbol{\omega} \times \mathbf{v}$.

3.3 | Helmholtz's solver

This section describes an optimal complexity algorithm for solving Helmholtz's equation on the ball with Dirichlet or integral boundary conditions. Helmholtz's equation with Dirichlet boundary conditions, discretized using the ultraspherical spectral method¹⁸ in the Chebyshev–Fourier–Fourier basis, yields to a Sylvester matrix equation, which can be solved in optimal complexity³⁴. However, it is not clear whether solving Helmholtz's equation with integral conditions in optimal complexity

is possible in this basis. We then choose to represent functions and solve Helmholtz's equation in the Chebyshev-Spherical harmonic basis since spherical harmonics decouple the angular part of the Laplacian in spherical coordinates. This choice, associated with the ultraspherical spectral method, introduced in¹⁸, leads to a fast and optimal complexity Helmholtz solver. Note that the algorithm described in this section is also applicable to “higher-order” Helmholtz equations such as Eqs. (12)-(13) but the description of the numerical method becomes more complicated.

3.3.1 | Spatial discretization of Helmholtz's equation

Consider the following Helmholtz's equation on the ball

$$\nabla^2 u + K^2 u = f, \quad (19)$$

where ∇^2 stands for the laplacian and K is the wave number. We first begin by writing Eq. (19) in spherical coordinate using the change of variables $(x, y, z) = (r \cos \lambda \sin \theta, r \sin \lambda \sin \theta, r \cos \theta)$:

$$\frac{1}{r^2} \frac{\partial}{\partial r} \left(r^2 \frac{\partial u}{\partial r} \right) + \frac{1}{r^2 \sin \theta} \frac{\partial}{\partial \theta} \left(\sin \theta \frac{\partial u}{\partial \theta} \right) + \frac{1}{r^2 \sin^2 \theta} \frac{\partial^2 u}{\partial \lambda^2} + K^2 u = f, \quad (20)$$

where $r \in [-1, 1]$, $\lambda \in [-\pi, \pi]$, and $\theta \in [0, \pi]$. Note that the radial variable r has been “doubled-up” and extended from $[0, 1]$ to $[-1, 1]$ to remove the artificial boundary condition at $r = 0$ (see Section 3.1.1). Eq. (20) is then multiplied by r^2 to remove the singularity at the origin:

$$\frac{\partial}{\partial r} \left(r^2 \frac{\partial u}{\partial r} \right) + \frac{1}{\sin \theta} \frac{\partial}{\partial \theta} \left(\sin \theta \frac{\partial u}{\partial \theta} \right) + \frac{1}{\sin^2 \theta} \frac{\partial^2 u}{\partial \lambda^2} + K^2 r^2 u = r^2 f. \quad (21)$$

Furthermore, we seek for a solution u expressed as the following CSH series

$$u(r, \theta, \lambda) \approx \sum_{k=0}^{n/2} \sum_{l=0}^{n/2} \sum_{m=-l}^l u_{klm} T_k(r) Y_l^m(\theta, \lambda). \quad (22)$$

Moreover, for $0 \leq l \leq n/2$ and $-l \leq m \leq l$, the spherical harmonic function of degree l and order m , Y_l^m , is an eigenvector of the surface laplacian ∇_1^2 with corresponding eigenvalue $-l(l+1)$ since

$$\nabla_1^2 Y_l^m := \frac{1}{\sin \theta} \frac{\partial}{\partial \theta} \left(\sin \theta \frac{\partial Y_l^m}{\partial \theta} \right) + \frac{1}{\sin^2 \theta} \frac{\partial^2 Y_l^m}{\partial \lambda^2} = -l(l+1) Y_l^m. \quad (23)$$

Then, Eq. (21) is equivalent to

$$\sum_{k=0}^{n/2} \sum_{l=0}^{n/2} \sum_{m=-l}^l u_{klm} \left[\frac{\partial}{\partial r} \left(r^2 \frac{\partial T_k(r)}{\partial r} \right) - l(l+1) T_k(r) + K^2 r^2 T_k(r) \right] Y_l^m = r^2 f. \quad (24)$$

The expression of the right hand side of Eq. (24) in the CSH basis reads

$$r^2 f(r, \lambda, \theta) = \sum_{k=0}^{n/2} \sum_{l=0}^{n/2} \sum_{m=-l}^l f_{klm} T_k(r) Y_l^m(\theta, \lambda).$$

We now fix $0 \leq l \leq n/2$, $-l \leq m \leq l$, and define the functions u_l^m , f_l^m on $r \in [-1, 1]$ by

$$u_l^m(r) = \sum_{k=0}^{n/2} u_{klm} T_k(r), \quad f_l^m(r) = \sum_{k=0}^{n/2} f_{klm} T_k(r).$$

The orthogonality of the spherical harmonics basis allows us to decouple Eq. (24) into the following second order ordinary differential equation:

$$\frac{\partial}{\partial r} \left(r^2 \frac{\partial u_l^m(r)}{\partial r} \right) + (K^2 r^2 - l(l+1)) u_l^m(r) = f_l^m(r), \quad r \in [-1, 1]. \quad (25)$$

This equation is solved using the ultraspherical spectral method¹⁸ as it typically leads to almost banded linear systems and optimal complexity numerical solvers. Let X_l^m (resp. F_l^m) be the vector of Chebyshev coefficients $(u_{klm})_{0 \leq k \leq n/2}$ (resp. $(f_{klm})_{0 \leq k \leq n/2}$) and A_l be the sparse and banded matrix representing the operator $u \mapsto \frac{\partial}{\partial r} \left(r^2 \frac{\partial u}{\partial r} \right) + (K^2 r^2 - l(l+1))u$ from the Chebyshev basis T to the ultraspherical $C^{(2)}$ basis. This transforms Eq. (25) into a linear system with an unknown column of Chebyshev coefficients X_l^m :

$$A_l X_l^m = F_l^m. \quad (26)$$

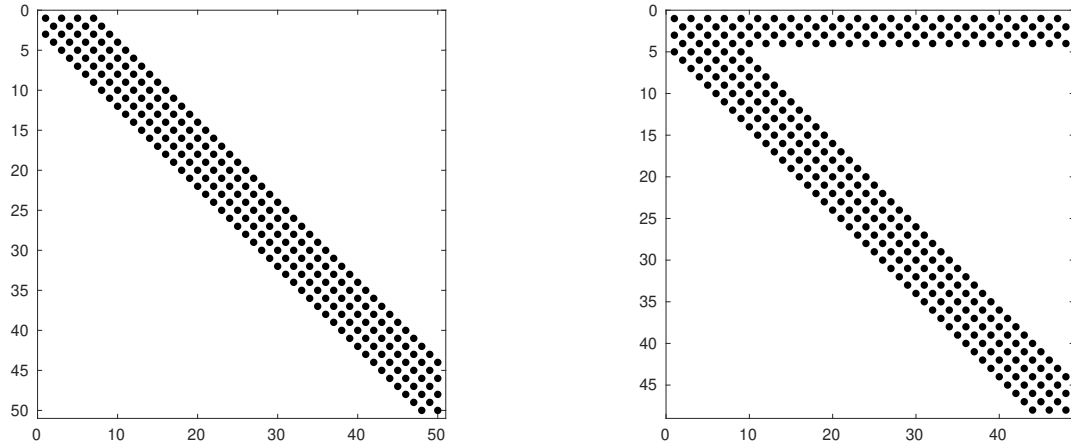


FIGURE 3 Left: Sparsity structure of the matrix A_l for $0 \leq l \leq n$. Right: Sparsity structure of the almost banded linear system after adding the boundary conditions.

Fig. 3 (left) shows the sparsity pattern of the matrix A_l , which is a sparse and banded matrix with bandwidth two. However, A_l is not a full rank matrix because the linear system (26) does not have a unique solution as Eq. (25) is a second-order ODE. We then have to modify the matrix A_l to remove degrees of freedom using Dirichlet or integral conditions (see Sections 3.3.2 and 3.3.3).

3.3.2 | Dirichlet conditions

We now consider Helmholtz's equation (19) with Dirichlet boundary conditions

$$u|_{\partial\Omega} = g,$$

where g is a smooth function defined on the unit sphere. g can be represented as a spherical harmonics series

$$g = \sum_{l=0}^{n/2} \sum_{m=-l}^l g_{lm} Y_l^m.$$

The boundary conditions decouple as well as the Helmholtz's equation in the CSH basis (see Section 3.3.1) and we obtain the following well-posed problem,

$$\frac{\partial}{\partial r} \left(r^2 \frac{\partial u_l^m}{\partial r} \right) + (K^2 r^2 - l(l+1)) u_l^m = f_l^m, \quad (27a)$$

$$u_l^m|_{r=1} = g_{lm}, \quad u_l^m|_{r=-1} = (-1)^l g_{lm}. \quad (27b)$$

Eq. (27a) is expressed as a ill-posed linear system (see Eq. (26)) in the unknown X_l^m , which represents the Chebyshev coefficients of the one-dimensional function u_l^m . Likewise, we express Eq. (27b) as a linear condition on X_l^m ,

$$\begin{pmatrix} 1 & 1 & 1 & 1 & \cdots \\ 1 & -1 & 1 & -1 & \cdots \end{pmatrix} X_l^m = \begin{pmatrix} g_{lm} \\ (-1)^l g_{lm} \end{pmatrix}. \quad (28)$$

Incorporating the Dirichlet boundary conditions (28) into Eq. (26) changes it to a sparse and almost banded linear system, which can be solved in $\mathcal{O}(n)$ operations using an algorithm based on a QR factorization¹⁸. The resulting linear system's sparsity pattern is shown in Fig. 3 (right). Finally, solving Helmholtz's equation with Dirichlet boundary conditions requires $\mathcal{O}(n^3)$ operations.

Fig. 4 shows a computed solution to the Helmholtz's equation $\nabla^2 u + u = (1 - (x^2 + y^2 + z^2)) \cos(10x + 5y)^2$ with zero Dirichlet boundary conditions and confirms the optimal complexity of the solver in the CSH basis.

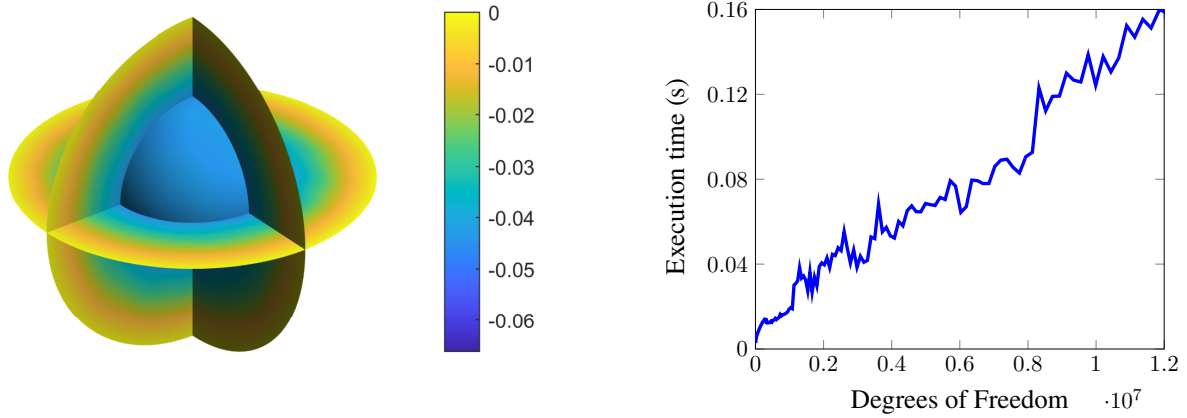


FIGURE 4 Left: Solution to the Helmholtz's equation $\nabla^2 u + u = (1 - (x^2 + y^2 + z^2)) \cos(10x + 5y)^2$ with homogeneous Dirichlet boundary conditions. Right: Execution time for the Helmholtz solver in the CSH basis with Dirichlet boundary conditions.

3.3.3 | Integral conditions

In this section, we consider Helmholtz's equation of the form

$$\nabla^2 u + K^2 u = f \quad (29)$$

with the integral conditions defined in Section 2.3.2. After explaining the discretization of the integral conditions in the Chebyshev-Spherical harmonic basis, we describe an optimal complexity algorithm to solve Eq. (29).

The integral conditions read (see Section 2.3.2):

$$\int_{\Omega} ru \partial_{rr}(rT_{\eta})^* dx = - \int_{\partial\Omega} \nabla_1 p \cdot \nabla_1 T_{\eta}^* ds, \quad (30)$$

where p is a surface potential defined in Section 2.3 and T_{η} is any harmonic function on the ball. Then, T_{η} satisfies

$$\nabla^2 T_{\eta} = 0, \quad T_{\eta}|_{\partial\Omega} = \alpha, \quad (31)$$

where α is an arbitrary smooth function on the sphere. We write α as a series of spherical harmonics

$$\alpha(\lambda, \theta) = \sum_{l=0}^{+\infty} \sum_{m=-l}^l \alpha_{ml} Y_l^m(\lambda, \theta),$$

which transforms the integral conditions into

$$\int_{\Omega} ru \partial_{rr}(rT_{\eta}^{m,l})^* dx = - \int_{\partial\Omega} \nabla_1 p \cdot \nabla_1 T_{\eta}^{m,l*} ds, \quad l \in \mathbb{N}, \quad -l \leq m \leq l, \quad (32)$$

where $T_{\eta}^{m,l}$ denotes the solution to Laplace's equation with Dirichlet boundary conditions Y_l^m , i.e.,

$$\nabla^2 T_{\eta}^{m,l} = 0, \quad T_{\eta}^{m,l}|_{\partial\Omega} = Y_l^m. \quad (33)$$

Laplace's equation in spherical coordinates reads

$$\frac{1}{r^2} \frac{\partial}{\partial r} \left(r^2 \frac{\partial T_{\eta}^{m,l}}{\partial r} \right) + \frac{1}{r^2 \sin \theta} \frac{\partial}{\partial \theta} \left(\sin \theta \frac{\partial T_{\eta}^{m,l}}{\partial \theta} \right) + \frac{1}{r^2 \sin^2 \theta} \frac{\partial^2 T_{\eta}^{m,l}}{\partial \lambda^2} = 0. \quad (34)$$

Since spherical harmonics are eigenvectors of the spherical Laplacian ∇_1^2 (see Eq. (23)), they decouple Eq. (33). Hence, $T_{\eta}^{m,l}$ can be written as $T_{\eta}^{m,l} = R_l^m Y_l^m$, where R_l^m is a function of the radial variable r to be determined by solving Eq. (34). Then, R_l^m is a solution to the following ordinary differential equation,

$$\frac{\partial}{\partial r} \left(r^2 \frac{\partial R_l^m}{\partial r} \right) - l(l+1)R_l^m = 0,$$

whose solutions can be expressed as $R_l^m(r) = Ar^l + Br^{-(l+1)}$ for A, B are real constants. According to Eq. (33), R_l^m is a smooth function on the ball and $R_l^m(1) = 1$, which implies $A = 1$ and $B = 0$. Hence, the solution to Eq. (33) is $T_{\eta}^{m,l} = r^l Y_l^m$.

Finally, after integrating by parts the right hand side of Eq. (30), the integral conditions become

$$\int_{\Omega} ru \partial_{rr} (r T_{\eta}^{m,l})^* dx = \int_{\partial\Omega} p \nabla_1^2 T_{\eta}^{m,l*} ds, \quad l \in \mathbb{N}, \quad -l \leq m \leq l. \quad (35)$$

Eq. (35) is discretized using the expression of u in the CSH basis and the spherical harmonics expansion of p ,

$$u = \sum_{k=0}^{+\infty} \sum_{l=0}^{+\infty} \sum_{m=-l}^l u_{klm} T_k Y_l^m, \quad f = \sum_{l=0}^{+\infty} \sum_{m=-l}^l p_{lm} Y_l^m. \quad (36)$$

Moreover, thanks to the orthonormality of the spherical harmonics basis, the left hand side of Eq. (35) is equivalent to

$$\int_{\Omega} ru \partial_{rr} (r T_{\eta}^{m,l})^* dx = \int_0^1 r \sum_{k=0}^{+\infty} u_{klm} T_k(r) \partial_{rr} (r^{l+1}) r^2 dr = l(l+1) \sum_{k=0}^{+\infty} \left(\int_0^1 r^{l+2} T_k(r) dr \right) u_{klm}, \quad (37)$$

for every integer l and $-l \leq m \leq l$. Likewise, the right hand side of Eq. (35) leads us to the following equality,

$$\int_{\partial\Omega} p \nabla_1^2 T_{\eta}^{m,l*} ds = -l(l+1) p_{lm}, \quad (38)$$

since the spherical harmonic Y_l^m is an eigenvector of the surface Laplacian ∇_1^2 with eigenvalue $-l(l+1)$. By combining Eqs. (37) and (38), we obtain the discretized formulation of the integral conditions:

$$\sum_{k=0}^{+\infty} \left(\int_0^1 r^{l+2} T_k(r) dr \right) u_{klm} = -p_{lm}, \quad l > 0, \quad -l \leq m \leq l.$$

However, u is written as a finite CSH series (see Eq. (22)), which leads to the following finite formulation of the integral conditions,

$$\sum_{k=0}^{n/2} \left(\int_0^1 r^{l+2} T_k(r) dr \right) u_{klm} = -p_{lm}, \quad 1 \leq l \leq n, \quad -l \leq m \leq l. \quad (39)$$

Eq. (39) is not defined for $l = 0$ because the solution to Helmholtz's equation with integral conditions is unique up to the addition of an arbitrary function of r . Hence, we impose $u_{k00} = 0$ for $0 \leq k \leq n/2$ to ensure the uniqueness of the solution to Eq. (29).

The integrals in Eq. (39) are computed via Clenshaw–Curtis quadrature by evaluating the Chebyshev polynomials T_0, \dots, T_n at Chebyshev nodes using Clenshaw's algorithm³⁵. This allows us to reformulate Eq. (39) as a linear condition on $X_l^m = (u_{klm})_k$,

$$B_l X_l^m = -p_{lm}. \quad (40)$$

According to Section 3.3.2, this condition can be enforced in the linear system Eq. (26):

$$A_l X_l^m = F_l^m,$$

by replacing the last row of A_l by the integral row condition B_l . Then, a permutation of the last row with the first row makes it close to upper triangular (see Fig. 3). Finally, Helmholtz's equation with integral conditions is solved in $\mathcal{O}(n^3)$ operations in the CSH basis as inverting this linear system demands $\mathcal{O}(n)$ operations for $1 \leq l \leq n/2$ and $-l \leq m \leq l$.

4 | NUMERICAL EXAMPLES

4.1 | Convergence test and execution time

First, we conduct a convergence test of the algorithm presented in Section 3 and solve the NS equations (written in vorticity form) on the unit ball:

$$\begin{aligned} \nabla^2 \psi &= -\omega, \\ \frac{\partial \omega}{\partial t} - \frac{1}{Re} \nabla^2 \omega &= -\nabla \times (\omega \times v), \end{aligned}$$

for low Reynolds numbers, and boundary conditions for the velocity field given as

$$f = 0, \quad g = \cos \theta,$$

where

$$v|_{\partial\Omega} = \nabla_1 f + \Lambda_1 g = \sin(\theta) \hat{\lambda}, \quad (41)$$

and $\hat{\lambda}$ denotes the unit vector in the azimuthal direction. We use a smooth random initial vorticity vector field sampled from a Gaussian process with squared-exponential covariance kernel^{36,37}, a spatial discretization of $n = 100$, corresponding to 1.5×10^6 , and a time-step of $\Delta_t = 10^{-4}$. As $Re \rightarrow 0$, the velocity should converge to the velocity solution to the Stokes' equations with similar boundary conditions, given by $\mathbf{v}_{\text{Stokes}} = r \sin(\theta) \hat{\lambda}$. We perform 4 transient simulations of the NS equations with respective Reynolds number $Re \in \{1, 10^{-1}, 10^{-2}, 10^{-3}\}$ and report the error in the L^2 -norm between the velocity $\mathbf{v}(t)$ and $\mathbf{v}_{\text{Stokes}}$ in Fig. 5(a). We observe that the error decays to nearly machine precision as the simulation time t increases and that the velocity obtained converges to the solution to the Stokes's equation when $Re \rightarrow 0$ as expected. This behaviour shows the spectral accuracy of the solver resulting from the choice of the spatial discretization.

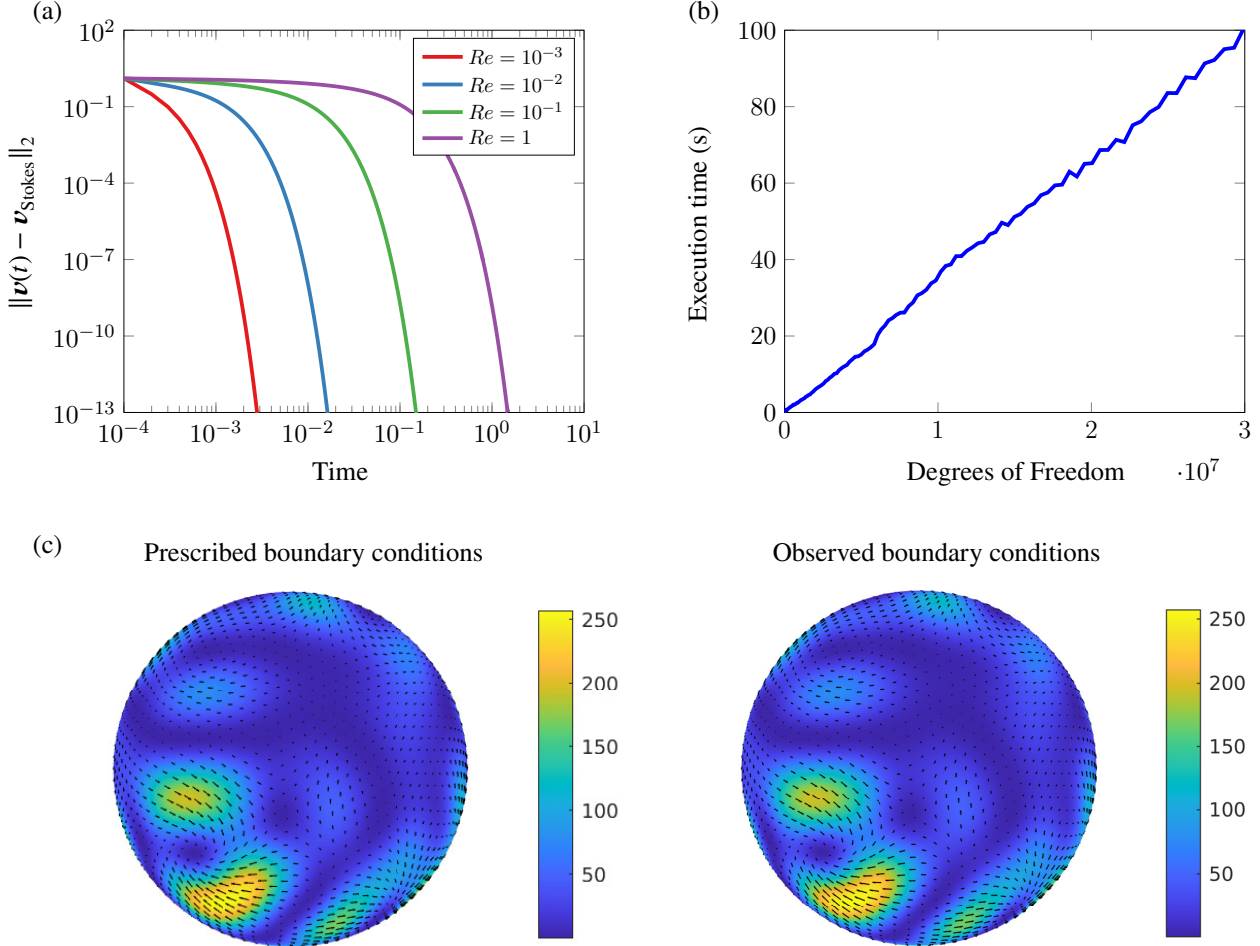


FIGURE 5 Convergence of the velocity field $\mathbf{v}(t)$ to the analytical solution $\mathbf{v}_{\text{Stokes}} = r \sin(\theta) \hat{\lambda}$ with respect to time for different Reynolds number (a). Computational timings of the algorithm for one time step with respect to the number of degrees of freedom (b). Test of the boundary conditions for the velocity field with prescribed velocity field at the surface and observed velocity at the boundary after one thousand time-steps (c).

Next, we perform several NS simulations with Reynolds number $Re = 70$, time-step $\Delta_t = 10^{-3}$, and boundary conditions given by Eq. (41). We vary the spatial discretization from $N = 11$ to $n = 271$, corresponding to a maximum number of degrees of freedom of $n = 3 \times 10^7$, and record the execution time¹ taken by the algorithm over the first 15 time-steps. Figure 5(b) displays the average computational time for one time-step as we increase the number of degrees of freedom and illustrate the optimal complexity of the method. Moreover, the NS equations can be solved on a ball with one million degrees of freedom in

¹Timings were performed on an Intel Xeon CPU E5-2667 v2 @ 3.30GHz using MATLAB R2019b without explicit parallelization.

a dozen seconds on a single CPU core. Finally, we highlight that the numerical algorithm presented in Section 3 fully decouple the NS equations into poloidal and toroidal equations, and all the subsequent operations (such as solving Helmholtz's equations, changing basis, and vector calculus) can be parallelized along one spatial direction, leading to nearly optimal scaling when using multiple CPU cores.

Finally, we test the imposition of the boundary conditions on the velocity field by performing a simulation at Reynolds number $Re = 1$, with time-step $\Delta_t = 10^{-3}$, a spatial discretization of $n = 101$, and smooth random surface potentials f and g (sampled from a Gaussian process). The left panel of Fig. 5(c) displays the prescribed velocity field: $\mathbf{v}_{\text{prescribed}} = \nabla_1 f + \Lambda_1 g$ and its magnitude at the surface of the sphere. In contrast, the right panel consists of the simulated velocity at the boundary after one thousand time-step. We observe that L^2 -norm of the difference between the two fields at the surface of the sphere is bounded by 10^{-8} .

4.2 | Active fluids simulation

We perform a simulation of the active fluid model in Eq. (1) with dimensionless parameters $\Gamma_0 = 1$, $\Gamma_2 = -8.13 \times 10^{-3}$, $\Gamma_4 = 1.65 \times 10^{-5}$. This choice of parameters represents active energy injection into the fluid at the scale corresponding to vortices with characteristic size $\Gamma = \pi(-2\Gamma_4/\Gamma_2)^{1/2} = 0.2$ and growth timescale $\tau = [\Gamma_2/(2\Gamma_4)(\Gamma_0 - \Gamma_2^2/(4\Gamma_4))]^{-1} = 2.76$ confined to a narrow active bandwidth $\kappa\Lambda = 0.12$, where $\kappa = [-\Gamma_2/\Gamma_4 - 2\sqrt{\Gamma_0/\Gamma_4}]^{1/2}$; the three characteristic scales (Λ, τ, κ) fully determine the resulting dynamics of the GNS model¹. As the boundary conditions for the velocity field on the unit ball, we use the no-slip boundary conditions $\mathbf{v}|_{\partial\Omega} = 0$, which corresponds to setting the velocity surface potentials to zero $f = g = 0$ (Section 2.3.2). To close the 6-th order Generalized Navier–Stokes Eq. (1), we additionally set the Laplacian and bi-Laplacian of the toroidal and poloidal scalars of the vorticity to zero on the boundary

$$\nabla^2 T_\omega(1, \lambda, \theta) = \nabla^4 T_\omega(1, \lambda, \theta) = 0, \quad \nabla^2 P_\omega(1, \lambda, \theta) = \nabla^4 P_\omega(1, \lambda, \theta) = 0. \quad (42)$$

This higher-order closure is motivated by similar closures on the vorticity field previously used in two-dimensional GNS systems^{38,39}. In simulations, the initial vorticity field is a smooth random vector field sampled from a Gaussian process. We use a spatial discretization parameter of $n = 100$, a time-step of $\Delta_t = 10^{-3}$, and run the simulation until $t = 75$, corresponding to 75000 time-steps and approximately 100 hours of execution time on a single core of a Intel Xeon CPU E5-2667 v2 @ 3.30GHz.

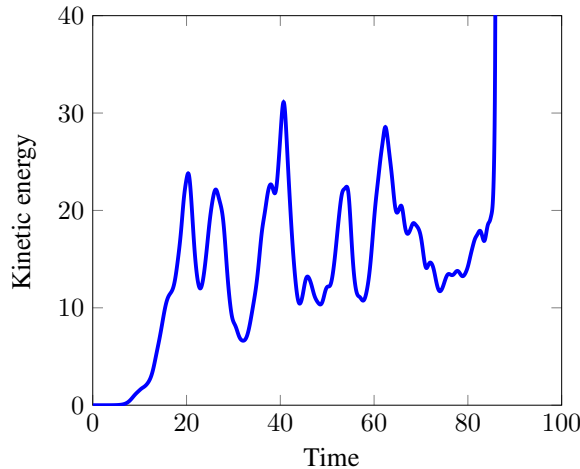


FIGURE 6 Kinetic energy of the active fluid simulation with respect to the time. The energy blow-up happens at time $t \approx 86$.

In a simulation, starting from a random field, the system builds up kinetic energy, defined as

$$\text{Kinetic energy} = \int_{B(0,1)} \mathbf{v} \cdot \mathbf{v} \, dx,$$

driven by the linear term proportional to Γ_2 in Eq. (1) (see Fig. 6). As the kinetic energy grows, the advective nonlinearity starts to impact the dynamics by mixing different wavelengths. As a result of this nonlinear coupling, the kinetic energy growth is eventually balanced by the dissipation at large and small wavelengths due to the viscous and hyper-viscous terms proportional

to Γ_0 and Γ_4 . Once this balance is reached, the system settles onto a statistically stationary state characterized by vortices of well-defined size (see Fig. 7 and a movie in Supplementary Material). The presence of vortices of well-defined size reflects our parameter choice to simulate a system with scale selection by settling a small value of the active bandwidth κ . At larger times, after a stationarity period, the kinetic energy grows rapidly again, and the system becomes unstable. We are unsure about the origin of this long-time instability. A possible reason is due to too small numerical discretization. Another reason for the blow-up is the boundary conditions in Eq. (42) being not dissipative enough, allowing the system to accumulate unlimited kinetic energy.

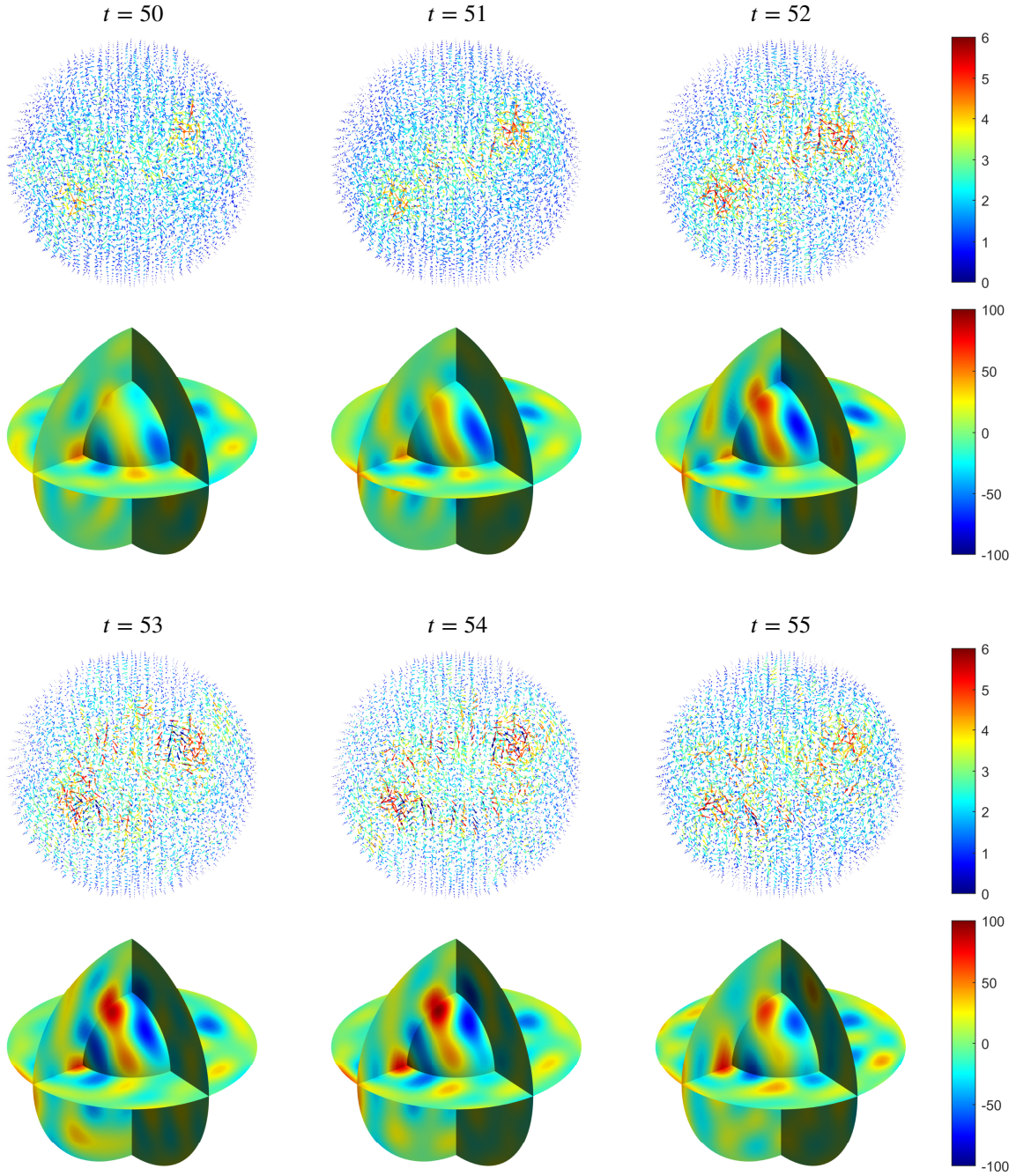


FIGURE 7 Snapshots of the velocity field and z component of the vorticity field during the active fluids simulation at times $t = 50, \dots, 55$.

5 | CONCLUSIONS

By exploiting the poloidal-toroidal decomposition of divergence-free vector fields, the Chebyshev–Fourier–Fourier and Chebyshev–Spherical harmonics bases, we developed an algorithm for solving the incompressible generalized NS equations on the ball with spectral accuracy and optimal complexity per time-step. Numerical experiments illustrated the linear scaling of the execution time with respect to the number of degrees of freedom and applied it to simulate an active fluids problem.

Our algorithm makes it straightforward to couple any surface dynamics with the interior dynamics once the user specifies separate evolution equations for the surface potentials of the compressible and rotational components of the velocity field on the boundary. Such active surface-driven flows could be important, for example, in studies of bulk flows driven by active stresses confined to a boundary^{40,41,42,43}.

The instability of the active fluid simulation and blow-up of the corresponding kinetic energy at large time can be investigated in the future by considering alternative higher-order boundary conditions to introduce more dissipation in the system. Another extension of this work is to parallelize the current implementation of the numerical method presented in this paper in order to reach the large spatial discretization required to simulate Navier–Stokes turbulences at large Reynolds number and study the stability of the technique in this regime.

ACKNOWLEDGEMENTS

We thank Jörn Dunkel for discussions and Keaton Burns for making us aware of performance benchmarks^{11,12}. This work was supported by the EPSRC Centre for Doctoral Training in Industrially Focused Mathematical Modelling (EP/L015803/1) in collaboration with Simula Research Laboratory. The third author was supported by the National Science Foundation grant DMS-1818757, DMS-1952757, and DMS-2045646, as well as the FACE Foundation.

References

1. Słomka J, Dunkel J. Spontaneous mirror-symmetry breaking induces inverse energy cascade in 3D active fluids. *Proc. Natl. Acad. Sci. USA* 2017; 114(9): 2119–2124.
2. Linkmann M, Boffetta G, Marchetti MC, Eckhardt B. Phase transition to large scale coherent structures in two-dimensional active matter turbulence. *Phys. Rev. Lett.* 2019; 122(21): 214503.
3. Chorin AJ. A numerical method for solving incompressible viscous flow problems. *J. Comput. Phys.* 1967; 2(1): 12–26.
4. Chorin AJ. Numerical solution of the Navier-Stokes equations. *Math. Comp.* 1968; 22(104): 745–762.
5. Guermond JL, Mineev P, Shen J. An overview of projection methods for incompressible flows. *Comput. Methods Appl. Mech. Eng.* 2006; 195(44): 6011–6045.
6. Burns KJ, Vasil GM, Oishi JS, Lecoanet D, Brown BP. Dedalus: A flexible framework for numerical simulations with spectral methods. *Phys. Rev. Res.* 2020; 2(2): 023068.
7. Lecoanet D, Vasil GM, Burns KJ, Brown BP, Oishi JS. Tensor calculus in spherical coordinates using Jacobi polynomials. Part-II: Implementation and examples. *J. Comput. Phys.: X* 2019; 3: 100012.
8. Vasil GM, Lecoanet D, Burns KJ, Oishi JS, Brown BP. Tensor calculus in spherical coordinates using Jacobi polynomials. Part-I: Mathematical analysis and derivations. *J. Comput. Phys.: X* 2019; 3: 100013.
9. Boronski P, Tuckerman LS. Poloidal–toroidal decomposition in a finite cylinder. I: Influence matrices for the magnetohydrodynamic equations. *J. Comput. Phys.* 2007; 227(2): 1523–1543.
10. Boronski P, Tuckerman LS. Poloidal–toroidal decomposition in a finite cylinder: II. Discretization, regularization and validation. *J. Comput. Phys.* 2007; 227(2): 1544–1566.

11. Marti P, Schaeffer N, Hollerbach R, et al. Full sphere hydrodynamic and dynamo benchmarks. *Geophys. J. Int.* 2014; 197(1): 119–134.
12. Matsui H, Heien E, Aubert J, et al. Performance benchmarks for a next generation numerical dynamo model. *Geochem. Geophys. Geosy.* 2016; 17(5): 1586–1607.
13. Backus G. Poloidal and toroidal fields in geomagnetic field modeling. *Rev. Geophys.* 1986; 24(1): 75–109.
14. Chandrasekhar S. *Hydrodynamic and Hydromagnetic Stability*. Courier Corporation . 1961.
15. Schmitt BJ, Wahl vW. Decomposition of solenoidal fields into poloidal fields, toroidal fields and the mean flow. Applications to the Boussinesq-equations. *Lect. Notes Math.* 1992; 1530: 291–305.
16. Quartapelle L, Valz-Gris F. Projection conditions on the vorticity in viscous incompressible flows. *Int. J. Numer. Methods Fluids* 1981; 1(2): 129–144.
17. Boullé N, Townsend A. Computing with Functions in the Ball. *SIAM J. Sci. Comput.* 2020; 42(4): C169–C191.
18. Olver S, Townsend A. A fast and well-conditioned spectral method. *SIAM Rev.* 2013; 55(3): 462–489.
19. Bhatia H, Norgard G, Pascucci V, Bremer PT. The Helmholtz–Hodge decomposition—A survey. *IEEE Trans. Visual. Comput. Graph.* 2013; 19(8): 1386–1404.
20. Canuto C, Hussaini MY, Quarteroni A, Thomas Jr A, others . *Spectral methods in fluid dynamics*. Springer Science & Business Media . 2012.
21. Karniadakis GE, Israeli M, Orszag SA. High-order splitting methods for the incompressible Navier-Stokes equations. *J. Comput. Phys.* 1991; 97(2): 414–443.
22. Kassam AK, Trefethen LN. Fourth-order time-stepping for stiff PDEs. *SIAM J. Sci. Comput.* 2005; 26(4): 1214–1233.
23. Kim J, Moin P. Application of a fractional-step method to incompressible Navier-Stokes equations. *J. Comput. Phys.* 1985; 59(2): 308–323.
24. Merilees PE. The pseudospectral approximation applied to the shallow water equations on a sphere. *Atmos.* 1973; 11(1): 13–20.
25. Townsend A, Wilber H, Wright GB. Computing with functions in spherical and polar geometries I. The sphere. *SIAM J. Sci. Comput.* 2016; 38(4): C403–C425.
26. Wilber H, Townsend A, Wright GB. Computing with functions in spherical and polar geometries II. The disk. *SIAM J. Sci. Comput.* 2017; 39(3): C238–C262.
27. Cooley JW, Tukey JW. An algorithm for the machine calculation of complex Fourier series. *Math. Comp.* 1965; 19(90): 297–301.
28. Driscoll TA, Hale N, Trefethen LN. *Chebfun Guide*. Pafnuty Publications . 2014.
29. Slevinsky RM. Fast and backward stable transforms between spherical harmonic expansions and bivariate Fourier series. *Appl. Comput. Harmon. Anal.* 2017.
30. Gentleman WM. Implementing Clenshaw–Curtis quadrature, I Methodology and Experience. *Comm. ACM* 1972; 15(5): 337–342.
31. Gentleman WM. Implementing Clenshaw–Curtis quadrature, II Computing the Cosine Transformation. *Comm. ACM* 1972; 15(5): 343–346.
32. Mason JC, Handscomb DC. *Chebyshev Polynomials*. CRC Press . 2002.
33. Kirby RM, Karniadakis GE. De-aliasing on non-uniform grids: algorithms and applications. *J. Comput. Phys.* 2003; 191(1): 249–264.

34. Fortunato D, Townsend A. Fast Poisson solvers for spectral methods. *IMA J. Numer. Anal.* 2020; 40(3): 1994–2018.
35. Trefethen LN. *Approximation Theory and Approximation Practice*. SIAM . 2013.
36. Filip S, Javeed A, Trefethen LN. Smooth random functions, random ODEs, and Gaussian processes. *SIAM Rev.* 2019; 61(1): 185–205.
37. Rasmussen CE, Williams C. *Gaussian processes for machine learning*. MIT Press . 2006.
38. Słomka J, Dunkel J. Geometry-dependent viscosity reduction in sheared active fluids. *Phys. Rev. Fluids* 2017; 2(4): 043102.
39. Słomka J, Townsend A, Dunkel J. Stokes’ second problem and reduction of inertia in active fluids. *Phys. Rev. Fluids* 2018; 3(10): 103304.
40. Mickelin O, Słomka J, Burns KJ, et al. Anomalous chained turbulence in actively driven flows on spheres. *Phys. Rev. Lett.* 2018; 120(16): 164503.
41. Shankar S, Bowick MJ, Marchetti MC. Topological sound and flocking on curved surfaces. *Phys. Rev. X* 2017; 7(3): 031039.
42. Supekar R, Heinonen V, Burns KJ, Dunkel J. Linearly forced fluid flow on a rotating sphere. *J. Fluid Mech.* 2020; 892.
43. Rank M, Voigt A. Active Flows on Curved Surfaces. *arXiv preprint arXiv:2102.03098* 2021.

